Bidirectional Counting of Single Electrons

T. Fujisawa[1,2,*], T. Hayashi[1], R. Tomita[1,2], and Y. Hirayama[1,3,4]

[1]*NTT Basic Research Laboratories, NTT Corporation,*
3-1 Morinosato-Wakamiya, Atsugi, 243-0198, Japan
[2]*Tokyo Institute of Technology, 2-12-1 Ookayama, Meguro-ku, Tokyo, 152-8551, Japan*
[3]*SORST-JST, 4-1-8 Honmachi, Kawaguchi, 331-0012, Japan*
[4]*Department of Physics, Tohoku University, Sendai, Miyagi, 980-8578, Japan*
[*]*To whom correspondence should be addressed. E-mail: fujisawa@nttbrl.jp.*

(Dated: May 8, 2006)

A bidirectional single-electron counting device is demonstrated, in which individual electrons flowing in forward and reverse directions through a double quantum dot are detected with a quantum point contact acting as a charge sensor. A comprehensive statistical analysis in the frequency and time domains and of higher-order moments of noise reveals anti-bunching correlation in single-electron transport through the device itself. The device is also demonstrated as an atto-ammeter to investigate extremely low current flow, which cannot be accessed by existing current meters.

Similar to the photon counting useful for detecting a faint light and characterizing nontrivial photon statistics [1], electron counting is expected to provide a sensitive ammeter and deep insights into correlated transport [3, 2]. In contrast to photon counting, in which only incoming photons are considered, back-scattering events occur frequently in electron transport, making bidirectional counting essential for a full understanding of its statistics. Conventional current noise measurements are successful for characterizing correlated transport [3, 4], such as the sub-Poissonian statistics in single-electron tunneling [5] and fractional quantum Hall effect [6, 7] have been investigated. However, the second-order noise measurements are restricted to strongly non-equilibrium conditions where transport can be considered unidirectional. In addition, these measurements cannot determine correlations of a few electrons, as existing current meters require the movement of millions of electrons. Recently, individual single-electron transport through a quantum dot has been investigated in real time using an integrated charge detector [8–11], but single-dot charge detection cannot determine the direction of the transport. We demonstrate a bidirectional single-electron counting (B-SEC) device, in which individual electrons tunneling through a double quantum dot (DQD) are detected with a charge sensor made of a quantum point contact (PC). Statistical analysis of forward and reverse tunneling events allows us to determine all parameters that describe the system. We find that two forward tunneling events never occur consecutively, which reveals anti-bunching correlation in the single-electron transport. The third-order noise is insensitive to thermal fluctuations, which allows us to extract the correlation effect even in a nearly equilibrium condition. These statistical methods can also be used to investigate extremely small current from an external test device.

The operation of our B-SEC device is based on charge detection in a DQD in the Coulomb blockade regime, where higher-order tunneling processes can be safely neglected [12]. As shown schematically in Fig. 1A, the device consists of a DQD (dots L and R) and a PC for charge detection. The PC is asymmetrically coupled to the dots (stronger to dot L), so that the current through the PC, I_{PC}, depends differently on the respective electron numbers (n, m) in dots L and R [13, 14]. The current through the DQD results in temporal changes in the electron numbers (n, m), which appear as fluctuations in the PC current, as shown in Fig. 1B. By observing transitions between $(1, 0)$ and $(0, 1)$ states, the current across the central barrier, I_C, can be regarded as a train of single-electron pulses, as shown in Fig. 1C.

Figure 1D shows a scanning electron micrograph (SEM) of a B-SEC device fabricated in an AlGaAs/GaAs heterostructure. The application of appropriate negative voltages on metal gates (gold regions) depletes conductive electrons nearby and forms the integrated device in a desired action [8]. The PC is adjusted in the tunneling regime, where I_{PC} is sensitive to the charge distribution around the PC. The current, $\langle I_{PC} \rangle \sim 12$ nA on average at an excitation voltage $V_{PC} = 0.8$ mV, changes by a few percent depending on the charge state of the DQD. Charge state (n, m) of the DQD can be controlled by voltages V_L and V_R respectively applied to gates G_L and G_R, and the average current $\langle I_{PC} \rangle$ shown in Fig. 2A indicates four discrete values depending on (n, m). Clear separation of $(0, 0)$ and $(1, 1)$ domains indicates an electrostatic coupling energy of ~ 200 μeV for the DQD [15]. Similar patterns are observed in a wide range of the V_L-V_R plane, and a specific region, where all the tunneling rates of the DQD are within the bandwidth (about 10 kHz) of the current amplifier used to measure I_{PC}, is chosen. Then, individual tunneling events can be clearly
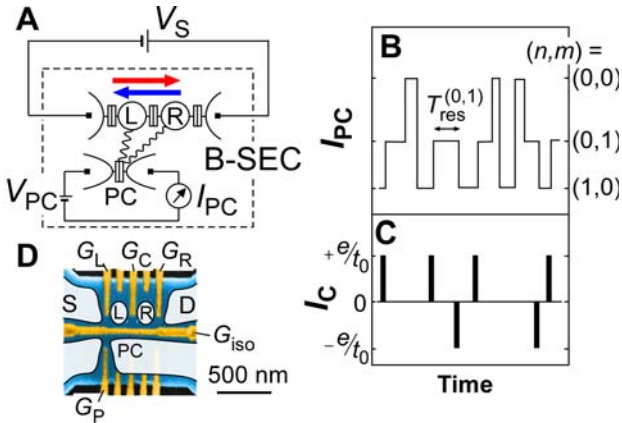
FIG. 1: B-SEC device. **(A)** The B-SEC device consists of a double dot (L and R) and a charge detector (PC). The double boxes represent tunneling barriers, and wavy lines illustrate Coulomb interaction. **(B)** Schematic fluctuation of detector current, I_{PC}, which corresponds to charge state (n, m) with n and m excess electrons respectively in dot L and R. **(C)** Pulsed current across the central barrier, I_C. Each current pulse with height e/t_0 and time resolution t_0 of the measurement represent transport of elementary charge e. **(D)** Colored SEM image (blue and black respectively for unetched and etched semiconductor surface, gold for metal gates, and white for conductive regions) of a control device fabricated using standard lithographic techniques. The double dot (L and R) and PC are formed by applying negative voltages to the gates. All measurements were performed at 35 mK at zero magnetic field.

visible in the time domain, as shown in Fig. 2B. The three-level fluctuation observed at charge triple points E and H, the two-level fluctuation between $(1, 0)$ and $(0, 1)$ at M, and the absence of fluctuation in blockade region B, are consistent with expectations.

We record I_{PC} traces over a period $T_p = 1.3$ s with a time resolution of $t_0 = 20$ μs and digitize the current into four values, corresponding to the (n, m) states of interest, with an appropriate filtering and threshold. If required, a group of many (up to 50) traces are used to obtain reliable statistics. All information needed for characterizing the transport can be obtained from the statistics. The residence time $T_{res}^{(n,m)}$, defined as how long the QD stays in a particular charge state (n, m) before changing to another state (See Fig. 1B for example), is a stochastic quantity and takes a random value every time, as shown in Fig. 2C. The data is taken in the non-linear conductance regime at a positive bias voltage $V_S = 300$ μV. The exponential distribution is observed for all charge states, indicating a random Poisson process characterized by a single lifetime $\tau_{nm} = \langle T_{res}^{(n,m)} \rangle$[8, 16], which is related to the sum of all possible tunneling rates $\Gamma_{nm \to ij}$ from (n, m) to (i, j), i.e., $\tau_{nm}^{-1} = \sum_{i,j} \Gamma_{nm \to ij}$. One can also count the number of transition events $N_{nm \to ij}$ from (n, m) to (i, j), which should be proportional to the rates by the relation $N_{nm \to ij} = p_{nm}^0 \Gamma_{nm \to ij} T_p$, where p_{nm}^0 is the occupation probability for (n, m) in a steady condition. By solving these relations, all relevant rates $\Gamma_{nm \to ij}$ and populations p_{nm}^0 can be determined.

Figure 2D shows $N_{nm \to ij}$ obtained from the same data set. The transport is dominated by a cyclic transition (shown by red arrows) from $(1, 1)$ through $(1, 0)$ to $(0, 1)$ and back to $(1, 1)$, which carries an electron from the left to the right. Note that non-negligible reverse processes (blue arrows) are also revealed in the present measurements. The very small counting rate (< 30 cps for the transitions involving $(0, 0)$ state) is attributed to noise in the PC current (dark counting) and should thus be disregarded; transitions between $(0, 0)$ and $(1, 1)$ are unphysical in the sequential tunneling regime. We should note that, due to the finite bandwidth, our measurement fails to count very fast successive transitions within 100 μs. These effects are all minor and do not affect our analysis. The obtained rates $\Gamma_{nm \to ij}$ are summarized in Fig. 2E.

We performed similar analysis at various points in the $V_L - V_R$ plane, and investigated how the forward and reverse tunneling rates change. We first examine dot-lead tunneling across the left barrier by comparing $\Gamma_{01 \to 11}$ and $\Gamma_{11 \to 01}$. They are plotted in Fig. 2F as a function the electrochemical potential, $\mu = E_{01} - E_{11}$, where E_{nm} is the total energy of (n, m) state [15]. The dependence can be well fitted with solid lines by considering the Fermi distribution in the electrode with an electron temperature of $T_e = 130$ mK in the lead [17]. The behaviors of the forward and reverse rates are almost symmetric with respect to $E_{10} = E_{11}$ (dashed line). The small
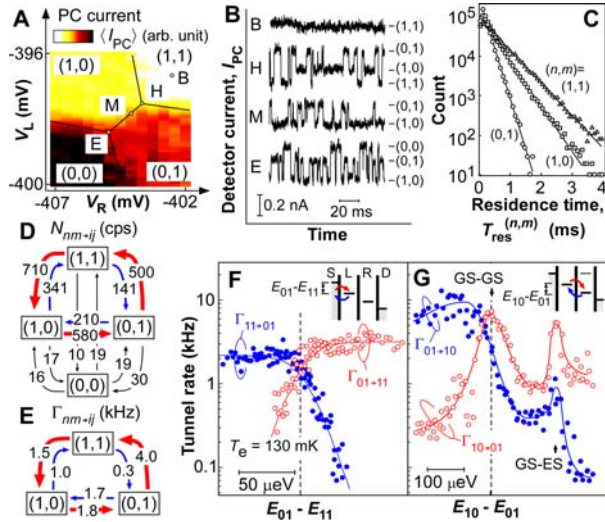
FIG. 2: Statistics of charge fluctuation in a DQD. **(A)** Color plot of the averaged PC current, $\langle I_{PC}\rangle$, in the $V_L - V_R$ plane measured at $V_S = 0$ and $V_{PC} = 0.8$ mV, with a stability diagram (n,m) of the DQD. An appropriate linear function of V_L and V_R is subtracted from the raw data to remove electrostatic coupling from the gates. **(B)** Fluctuation of I_{PC} measured at some points shown in **A**. Typically $\langle I_{PC}\rangle \sim 12$ nA. **(C)** Distribution of the residence time T_{res} for $(0,1)$, $(1,0)$ and $(1,1)$ states. **(D)** An example of the number of transition events $N_{nm\to ij}$. **(E)** An example of tunneling rates $\Gamma_{nm\to ij}$. The same data set measured at $V_S = 300$ μV around point α in Fig. 3A is used for **C**, **D** and **E**. **(F and G)** Forward and reverse rates across left **(F)** and central **(G)** barriers. Insets show energy diagrams of the DQD with corresponding tunnel processes. Obtained rates at $V_S = 300$ μV and various V_L and V_R points are plotted as a function of chemical potential, $E_{01} - E_{11}$ in **F** and $E_{10} - E_{01}$ in **G**. Solid lines in **F** are fitted with $T_e = 130$ mK, while solid lines in **G** are guides for the eye. Arrows in **G** represent resonances of the ground state (GS) of one dot to the ground and excited states (ES) of the other dot.

difference of a factor ~ 1.5 between the maximum saturated rates for the forward and reverse tunneling may be related to spin degeneracy; a factor-2 difference is expected for transitions between different charge states having total spins of 0 and 1/2 [18]. The dot-lead tunneling shows detailed balancing, in which the ratio of forward and reverse rates is determined by the electrochemical potential, $\Gamma_{01\to 11}/\Gamma_{11\to 01} = \exp[\mu/kT_e]$, up to degeneracy. In contrast, interdot tunneling rates $\Gamma_{01\to 10}$ and $\Gamma_{10\to 01}$ measure how frequently the system absorbs or emits energy from or to the environment [19]. As shown in Fig. 2G, the rates deviate from the symmetric dependence in the whole range across some peaks (indicated by arrows) associated with alignments of discrete energy levels in the dots. Violation of detailed balancing implies strong non-equilibrium excitation under back action from the PC detector [20].

Although each tunneling process characterized by $\Gamma_{nm\to ij}$ is Poison random, Coulomb interaction prohibits double occupancy in a small island and correlates the overall electron transport. Charge transport in the sequential tunneling regime can be described by the rate equation $\frac{d}{dt}\mathbf{p}(t) = \mathbf{M}\mathbf{p}(t)$, where $\mathbf{p}(t)$ is an array of time-dependent occupation probabilities $\{p_{nm}(t)\}$ [21]. The matrix $\mathbf{M}$ describes the transition rates consisting of diagonal and off-diagonal terms, $-\tau_{nm}^{-1}$ and $\Gamma_{nm\to ij}$, respectively. As we have already obtained $\mathbf{M}$ as in Fig. 2E, we can calculate the expected average current, noise spectrum [21], and higher-order moments of noise [22], which are more suitable for describing the correlated transport. These statistics can be obtained by analyzing the pulsed current (conserved quantity), which is more versatile even when complete information, like $\mathbf{M}$, is not available.

Here, we define three pulsed currents, I_L, I_C and I_R, which exhibit B-SEC respectively at the left, central, and right barriers. They are obtained by considering the corresponding tunneling processes as discussed for I_C in Fig. 1C. The average currents obtained for a long period $T_p = 1.3$ s always coincide with each other, i.e., $\langle I_L\rangle = \langle I_C\rangle = \langle I_R\rangle$, as a result of current conservation. Figure 3A shows the average current $\langle I\rangle$ in the $V_L - V_R$ plane. The triangular conductive regions at around E and H with a resonant tunneling peak on one side of the triangles are consistent with the energetics for transport through a DQD [15].

Noise power spectra, S_L, S_C and S_R, shown in the top panel of Fig. 3B, are obtained from numerical Fourier transforms of the corresponding pulsed currents. The spectra are qualitatively the same as those calculated from $\mathbf{M}$ (bottom panel of Fig. 3B) [21], indicating the validity of our statistical analysis. The enhanced spectrum in the high-frequency part (> 1 kHz, the characteristic frequency set by $\mathbf{M}$) is related to how frequently an electron experiences back-scattering across the barrier. The low-frequency part, identical for the three spectra, is almost flat except for excess dark-counting noise below 10 Hz. Background charge fluctuation (1/f noise), which
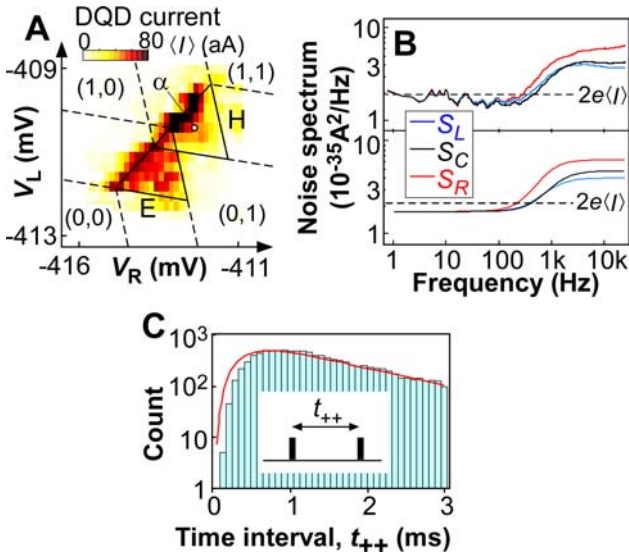
FIG. 3: Statistics of current at the left, central, and right barriers. **(A)** Average current $\langle I \rangle$ in the $V_L - V_R$ plane at $V_S = 300$ μV. Triangles, E and H, define conductive regions. **(B)** Noise power spectra of the current, S_L, S_C, and S_R. The upper panel shows the power spectrum of the pulsed current, while the lower panel shows the spectrum of the correlation function derived by solving rate equations. The dashed line shows full shot noise $2e\langle I \rangle$. **(C)** Distribution of the time interval between successive forward tunneling events in I_C. Solid line shows calculated occurrence of the conditional event derived from the corresponding rate equations. The inset illustrates the time interval, t_{++}. The same data set used for **B** and **C**, as well as for Figs. 2C-2E is taken in the nonlinear conductance regime (point α in **A**).

often dominates low-frequency noise, is significantly suppressed in our scheme. The noise level in the 10 - 100 Hz range is suppressed below full shot noise $2e\langle I \rangle$ (dashed line), indicating correlated transport [5]. In fact, we find that B-SEC provides better statistics that identify the anti-bunching correlation directly. Figure 3C shows the distribution of the time interval, t_{++}, between two successive forward current pulses. The distribution is no longer a simple exponential, and suppression of consecutive forward pulses at $t_{++} \sim 0$ (anti-bunching) is directly identified, consistent with a rate-equation calculation (solid line). Note that the broad peak in the distribution indicates quasi-periodical current as a precursor of single-electron tunneling oscillations [10].

We can extract other statistics often used in quantum optics, like electron (photon) number distribution [1, 2, 23]. The third-order moment of the distribution, which is called skewness, is of particular interest for its insensitivity to thermal distribution [24–26] and is considered to be a new tool for investigating correlated transport, valid even for nearly-equilibrium conditions. Gustavsson et al. used charge detection measurement on a single dot to identify correlated transport from its second- and third-order noise [11]. Taking advantage of bidirectional counting in our device, we have demonstrated that the third-order noise is insensitive to the thermal noise.

The electron number distribution of interest can be obtained in the zero-frequency limit, which has been discussed theoretically [22]. The current is averaged for a moderate averaging period $T_{avr} = 4$ ms, which is longer than the correlation time of the transport (about 0.3 ms, as seen in Fig. 3C). The distribution of the net electron number, N, transferred during the averaging time is plotted in Fig. 4A. The mean and variance of the distribution correspond to the average current, $\langle I \rangle = e\langle N \rangle/T_{avr}$, and second-order noise, $S = e^2\langle \delta N^2 \rangle/T_{avr}$, respectively, where $\delta N = N - \langle N \rangle$. The small asymmetric distribution indicates the presence of skewness and corresponding third-order noise, $C = e^3\langle \delta N^3 \rangle/T_{avr}$. The relative value to the full shot noise, $C/(e^2\langle I \rangle)$, measures the correlation of the transport [24, 27]. The ratio of 0.17 for Fig. 4A indicates anti-bunching correlation (< 1), consistent with the calculation (~ 0.2) based on Ref. [22]. In order to test how closely the measurement can be performed in the equilibrium condition at zero bias, the second- and third-order noise are plotted as a function of the bias voltage in Fig. 4B. Here, we have chosen the linear conductance region around the triple point H, where the current is restricted by one of the barriers (equivalent to the single barrier case for the noise). In this case, the second- and third-order noise should coincide with full shot noise $e\langle I \rangle$ and $e^2\langle I \rangle$, respectively, if other noise does not contribute. The second-order noise is significantly higher than $e\langle I \rangle$ at small voltage $V_S < 100$ μV, where the thermal noise is dominant ($k_B T_e = 15$ μeV). In contrast, the third-order noise follows $e^2\langle I \rangle$ in the whole range, and no additional noise is observed. This administrates that insensitivity
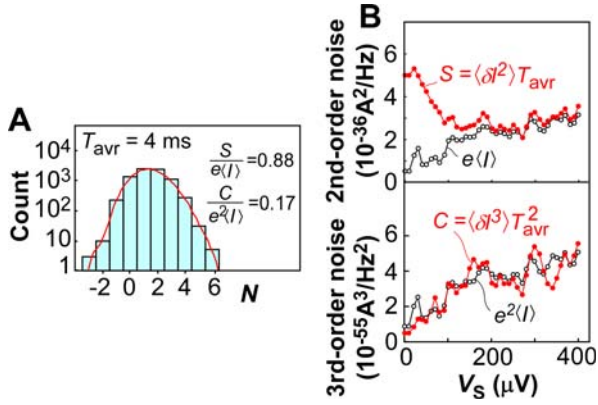
FIG. 4: **(A)** Electron number distribution for I_C. N is the net electron number transferred across the central barrier during the averaging time, $T_{avr} = 4$ ms. The same data set as for Fig. 2E is used. **(B)** Bias voltage dependence of second- and third-order noise in the linear conductance regime (around triple point H in the $V_L - V_R$ plane of Fig. 2A).
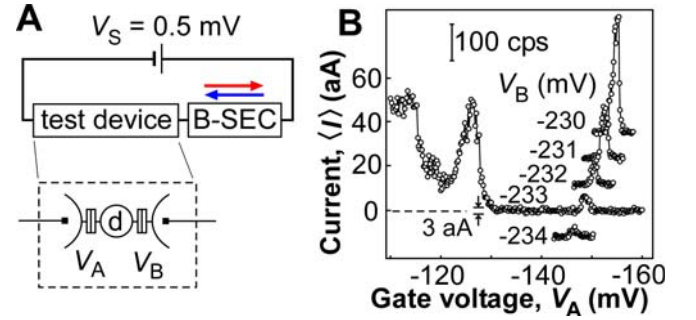

FIG. 5: Single electron counting for an external test device. **(A)** Measurement diagram with a QD (d) test device fabricated with the same technique as the B-SEC device. Tunneling rates of the two barriers on both sides of the QD can be controlled with voltages V_A and V_B. **(B)** Average current obtained from the B-SEC device. Current ranging from -10 to 50 aA can be measured with voltage drop of about 200 μV across the present B-SEC device. The observed Coulomb blockade peaks changes with V_B. Each trace is offset for clarity.

to thermal noise is desirable for measuring meaningful non-Gaussian noise even at high temperature.

The reverse problem of identifying unknown correlation would be useful in many cases. The top part of Fig. 5A illustrates a circuit for counting electrons from a test device. Although it is impossible to obtain all information about the test device, one can obtain useful information by means of time, frequency, and momentum analyses with a B-SEC device. For this purpose, the impedance of the B-SEC device should be smaller and its correlation time shorter than that of the test device [28]. Our B-SEC device can be applied to investigate extremely small current from a high-impedance test device, and this is precisely what conventional electronics cannot cover. We demonstrate the performance of our device as a current meter using another single QD as a test device as shown in Fig. 5A. The average current $\langle I \rangle$ obtained from the B-SEC device reasonably depends on two gate voltages (V_A and V_B) of the test device as shown in Fig. 5B, indicating that the observed Coulomb blockade peaks are associated with the test device. The noise level in the blockade region is 3 aA for 1.3-s averaging time, which is about three orders of magnitude smaller than that in conventional current meters.

The demonstrated B-SEC device enables various statistical analyses to characterize the correlation, and is also useful in investigating extremely small current. Integration with other mesoscopic electron devices, such as beam splitters or interferometers, would lead to various techniques for exploring non-trivial intensity correlation and entanglement in mesoscopic electron systems [29].

REFERENCES

[1] R. Loudon *The quantum theory of light* (Oxford, New York, 1973).

[2] L. S. Levitov, H. Lee, G. B. Lesovik, *J. Math. Phys.* **37**, 4845 (1996).

[3] *Quantum Noise in Mesoscopic Physics*, Yu. V. Nazarov Ed. (NATO Science Series II Vol. 97, Kluwer, Dordrecht, The Netherlands, 2003).

[4] Ya. M. Blanter, M. Büttiker, *Phys. Reports* **336**, 1 (2000).

[5] H. Birk, M. J. M. de Jong, C. Schönenberger, *Phys. Rev. Lett.* **75**, 1610 (1995).

[6] L. Saminadayar, D. C. Glattli, Y. Jin, B. Etienne, *Phys. Rev. Lett.* **79**, 2526 (1997).

[7] R. de-Picciotto et al., *Nature* **389**, 162 (1997).

[8] T. Fujisawa, T. Hayashi, Y. Hirayama, H. D. Cheong, Y. H. Jeong, *Appl. Phys. Lett.* **84,** 2343 (2004).

[9] W. Lu, Z. Ji, L. Pfeiffer, K. W. West, A. J. Rimberg, *Nature* **423,** 422 (2003).

[10] J. Bylander, T. Duty, P. Delsing, *Nature* **434,** 361 (2005).

[11] S. Gustavsson et al., *Phys. Rev. Lett.* **96**, 076605 (2006).

[12] *Single Charge Tunneling, Coulomb Blockade Phenomena in Nanostuctures*, H. Grabert, M. H. Devoret Eds., NATO ASI series B 294, (Plenum Press, New York, 1991).

[13] M. Field et al., *Phys. Rev. Lett.* **70**, 1311 (1993).

[14] J. R. Petta et al., *Science* **309,** 2180 (2005).

[15] W. G. van der Wiel et al., *Rev. Mod. Phys.* **75,** 1 (2003).

[16] N. G. van Kampen, *Stochastic Processes in Physics*

and Chemistry (Elsevier, 1992).

[17] D. H. Cobden, B. A. Muzykantskii, *Phys. Rev. Lett.* **75,** 4274 (1995).

[18] D. H. Cobden, M. Bockrath, P. L. McEuen, A. G. Rinzler, R. E. Smalley, *Phys. Rev. Lett.* **81,** 681 (1998).

[19] T. Fujisawa et al., Science **282**, 932 (1998).

[20] R. Aguado, L. P. Kouwenhoven, *Phys. Rev. Lett.* **84,** 1986-1989 (2000).

[21] S. Hershfield, J. H. Davies, P. Hyldgaard, C. J. Stanton, J. W. Wilkins, *Phys. Rev.* **B 47,** 1967 (1993).

[22] D. A. Bagrets, Yu. V. Nazarov, *Phys. Rev.* **B 67**, 085316 (2003).

[23] M. Ueda, *Phys. Rev.* **A 40**, 1096 (1989).

[24] L. S. Levitov, M. Reznikov, *Phys. Rev.* **B 70,** 115305 (2004).

[25] B. Reulet, J. Senzier, D. E. Prober, *Phys. Rev. Lett.* **91**, 196601 (2003).

[26] Yu. Bomze, G. Gershon, D. Shovkun, L. S. Levitov, M. Reznikov, *Phys. Rev. Lett.* **95**, 176601 (2005).

[27] G. Kießlich, P. Samuelsson, A. Wacker, E. Schöll, *Phys. Rev.* **B 73,** 033312 (2006).

[28] C. W. J. Beenakker, M. Kindermann, Yu. V. Nazarov, *Phys. Rev. Lett.* **90,** 176802 (2003).

[29] P. Samuelsson, E. V. Sukhorukov, and M. Büttiker, *Phys. Rev. Lett.* **92,** 026805 (2004).

[30] We thank L. S. Levitov, K. Muraki, Yu. V. Nazarov, Y. Tokura, M. Ueda, and Y. Yamamoto for valuable comments. This work was supported by the SCOPE from the Ministry of Internal Affairs and Communications of Japan, and by a Grant-in-Aid for Scientific Research from the JSPS.

Fig. 1. B-SEC device. **(A)** The B-SEC device consists of a double dot (L and R) and a charge detector (PC). The double boxes represent tunneling barriers, and wavy lines illustrate Coulomb interaction. **(B)** Schematic fluctuation of detector current, I_{PC}, which corresponds to charge state (n, m) with n and m excess electrons respectively in dot L and R. **(C)** Pulsed current across the central barrier, I_C. Each current pulse with height e/t_0 and time resolution t_0 of the measurement represent transport of elementary charge e. **(D)** Colored SEM image (blue and black respectively for unetched and etched semiconductor surface, gold for metal gates, and white for conductive regions) of a control device fabricated using standard lithographic techniques. The double dot (L and R) and PC are formed by applying negative voltages to the gates. All measurements were performed at 35 mK at zero magnetic field.

Fig. 2. Statistics of charge fluctuation in a DQD. **(A)** Color plot of the averaged PC current, $\langle I_{PC} \rangle$, in the $V_L - V_R$ plane measured at $V_S = 0$ and $V_{PC} = 0.8$ mV, with a stability diagram (n, m) of the DQD. An appropriate linear function of V_L and V_R is subtracted from the raw data to remove electrostatic coupling from the gates. **(B)** Fluctuation of I_{PC} measured at some points shown in **A**. Typically $\langle I_{PC} \rangle \sim 12$ nA. **(C)** Distribution of the residence time T_{res} for $(0, 1)$, $(1, 0)$ and $(1, 1)$ states. **(D)** An example of the number of transition events $N_{nm \to ij}$. **(E)** An example of tunneling rates $\Gamma_{nm \to ij}$. The same data set measured at $V_S = 300$ μV around point α in Fig. 3A is used for **C**, **D** and **E**. **(F and G)** Forward and reverse rates across left (**F**) and central (**G**) barriers. Insets show energy diagrams of the DQD with corresponding tunnel processes. Obtained rates at $V_S = 300$ μV and various V_L and V_R points are plotted as a function of chemical potential, $E_{01} - E_{11}$ in **F** and $E_{10} - E_{01}$ in **G**. Solid lines in **F** are fitted with $T_e = 130$ mK, while solid lines in **G** are guides for the eye. Arrows in **G** represent resonances of the ground state (GS) of one dot to the

ground and excited states (ES) of the other dot.

Fig. 3. Statistics of current at the left, central, and right barriers. **(A)** Average current $\langle I \rangle$ in the $V_L - V_R$ plane at $V_S = 300$ μV. Triangles, E and H, define conductive regions. **(B)** Noise power spectra of the current, S_L, S_C, and S_R. The upper panel shows the power spectrum of the pulsed current, while the lower panel shows the spectrum of the correlation function derived by solving rate equations. The dashed line shows full shot noise $2e\langle I \rangle$. **(C)** Distribution of the time interval between successive forward tunneling events in I_C. Solid line shows calculated occurrence of the conditional event derived from the corresponding rate equations. The inset illustrates the time interval, t_{++}. The same data set used for **B** and **C**, as well as for Figs. 2C-2E is taken in the nonlinear conductance regime (point α in **A**).

Fig. 4. **(A)** Electron number distribution for I_C. N is the net electron number transferred across the central barrier during the averaging time, $T_{avr} = 4$ ms. The same data set as for Fig. 2E is used. **(B)** Bias voltage dependence of second- and third-order noise in the linear conductance regime (around triple point H in the $V_L - V_R$ plane of Fig. 2A).

Fig. 5. Single electron counting for an external test device. **(A)** Measurement diagram with a QD (d) test device fabricated with the same technique as the B-SEC device. Tunneling rates of the two barriers on both sides of the QD can be controlled with voltages V_A and V_B. **(B)** Average current obtained from the B-SEC device. Current ranging from -10 to 50 aA can be measured with voltage drop of about 200 μV across the present B-SEC device. The observed Coulomb blockade peaks changes with V_B. Each trace is offset for clarity.